Postprint of: Sethy S. K., Ficek M., Sankaran K. J., Sain S., Tripathy A. R., Gupta S., Ryl J., Sinha Roy S., Tai N., Bogdanowicz R., Nitrogen-Incorporated Boron-Doped Nanocrystalline Diamond Nanowires for Microplasma Illumination, ACS Applied Materials & Interfaces Vol. 13, No 46 (2021), pp. 55678-55699, DOI: 10.1021/acsami.1c16507

Nitrogen-Incorporated Boron-doped Nanocrystalline Diamond Nanowires for Microplasma Illumination

Salila Kumar Sethy,† Mateusz Ficek,† Kamatchi Jothiramalingam Sankaran,* Sourav Sain, Anupam Ruturaj Tripathy, Shivam Gupta, Jacek Ryl, Susanta Sinha Roy, Nyan-Hwa Tai, and Robert Bogdanowicz*

ABSTRACT: Origin of nitrogen incorporated boron doped nanocrystalline diamond (NB-NCD) nanowires as a function of substrate temperature (*T*s) in $H_2/CH_4/B_2H_6/N_2$ reactant gases is systematically addressed. Because of *T*s a drastic modification in dimensional structure and microstructure and hence the several properties of the NB-NCD films. The NB-NCD films grown at low *T*s (400ºC) contain faceted diamond grains. The morphology changes to nano-sized diamond grains for NB-NCD films grown at 550ºC (or 700ºC). Interestingly, the NB-NCD films grown at 850ºC possess one-dimensional nanowire-like morphological grains. These nanowire-like NB-NCD films possess the co-existence of sp^3-diamond phase as well as sp^2-graphitic phase, where diamond nanowires surrounded by sp^2-graphitic phases at grain boundaries. The optical emission spectroscopy (OES) studies stated that the CN, BH and C_2 species in the plasma are the main factors for the origin of nanowire-like conducting diamond grains and the materialization of graphitic phases at the grain boundaries. Moreover, conducting atomic force microscopy studies reveal that the NB-NCD films grown at 850ºC show a large number of emission sites from the grains and the grain boundaries. While boron doping improved the electrical conductivity of the NCD grains, the nitrogen incorporation eased the generation of graphitic phases at the grain boundaries that afford conducting channels for the electrons, thus achieved a high electrical conductivity for the NB-NCD films grown at 850ºC. The microplasma devices using these nanowire-like NB-NCD films as cathode display superior plasma illumination properties with threshold field of 3300 V/μm, plasma current density of 1.04 mA/cm^2 with a supplied voltage of 520 V and a

lifetime stability of 520 min. The outstanding plasma illumination characteristics of these conducting nanowire-like NB-NCD films make them appropriate as cathodes and pave the way for the utilization of these materials in various microplasma device applications.

KEYWORDS: *diamond nanowires, boron doping, nitrogen incorporation, microplasma illumination, microstructural evolution, optical emission spectroscopy*

■ INTRODUCTION

The word "*miniaturization*" has developed an immense progress in the field of electronics, photonics and materials science. Particularly, micro-/nano-structured materials and miniaturized devices have afforded potential economic and technological benefits.[1,2] Microplasma device, one of the miniaturized devices, has received growing attention to the researchers because of its portability, cost, and robustness in a wide range of applications in plasma displays, plasma medicine, triboelectrics, nanomaterials' synthesis, gas treatment, etching processes, excimer sources, spectroscopy of gases, and analytical chemistry.[3,4] The term "microplasma" is usually utilized to refer low-temperature plasma discharges having dimensions of few micrometers to a few millimetres.[5] The plasma discharges generate a high sensitive environment that comprises of excited species, charged particles, photons, and radicals, and the reduced dimensions allow low-power sources with small footprints suitable for the combination in microsystems and also in portable devices. The microplasma devices are functioned under dielectric layer material, diverse electrodes, working ambient gas, relative electrode distance, pressure, driving voltage, temperature, frequency, and waveform.[6] Particulars of microplasma sources with various characteristics, their designimg, modes of action and probable applications have been hugely deliberated.[5,6] Even though many applications of microplasma devices have been developed, the glowing proficiency of the microplasma devices is still limited.

The construction of a cathode material that can proficiently eject electrons for the aim to improve the luminous efficiency of a microplasma device is of prime importance. The materials such as MgO, Al_2O_3, boron nitride, barium titanate, silicon, carbon nanotubes, graphene, ZnO were utilized as cathodes in microplasma devices.[7,8] Because of their poor stability, these materials cannot withstand in a harsh plasma environment for a longer duration. Hence, hunt for a suitable cathode material has begun, in which the material can enhance the plasma characteristics and increase the sustainability of plasma discharges. High proficiency to produce secondary electrons by means of plasma ion bombardment (i.e. large secondary electron emission coefficient), which can increase the sustainability of discharges, which is a key significance for the selection of cathode materials for microplasma devices.[9]

Due to high chemical inertness, high thermal conductivity, low sputtering yield, rigidity, insensitivity to numerous processing conditions, wide band gap and negative electron affinity characteristics, diamond thin films synthesized using chemical vapour deposition (CVD) systems usually exhibit a large secondary electron emission coefficient[10] and those are highly suitable as cathodes for microplasma devices.[11] Along with the above mentioned properties, diamond films should be electrically conducting to be an efficient cathode in microplasma devices. Using suitable dopants and impurities, it is practicable to synthesize electrically conducting diamond films and also the conductivity can be tailored related to the application requirement.[12,13]

Diamond films with micron-sized grains are designated as microcrystalline diamond (MCD) films, which possess high resistivity.[14] By the incorporation of nitrogen in CH_4/H_2 plasma, the grain size reduces from micron to nanosize ensuing the formation of nanocrystalline diamond (NCD) films. In addition, N_2 encourages graphitic phases at the grain boundaries that improves electrical conductivity and therefore improves the emission of electrons from NCD films.[15] It is proposed that the electrical conduction in the grain

boundaries is the main cause to improve electron emission characteristics of the nitrogen incorporated NCD films.[16] But the insulating nature of nanosized diamond grains still confines the electrical conduction to the grain boundaries and thus limits the electron emission characteristics of NCD films. Instead, doping boron in diamond films can render diamond grains conductive because boron atoms substitute sp^3-carbon atoms in the diamond lattice.[17] Substantial progress has been made in doping boron in diamond and achieved good electrical conductivity.[18] Gajewski *et al.*[19] stated that the conductivity of boron doped NCD films is because of holes not by electrons, signifying that grain boundaries are not the key factor for the electron transport in B-doped NCD films. However, the material that exists at the grain boundaries of boron doped NCD films is not examined yet. Also, the effect of N_2 incorporation on the evolution of morphology, bonding characteristics, microstructure and electrical conductivity of boron doped NCD films is still not evidently dealt with or revealed.

In this work, a methodology to synthesize nitrogen incorporated boron doped NCD (NB-NCD) films, with the purpose of developing an efficient cathode material for microplasma devices, is discussed. With the aim of achieving conducting carbon phases at each diamond grain boundaries (by the incorporation of N_2) between boron doped diamond grains, NB-NCD films were grown by varying the substrate temperatures with $H_2/CH_4/B_2H_6/N_2$-based microwave plasma-enhanced CVD (MWPECVD) system. Interestingly, the NB-NCD films grown at 850ºC possess one-dimensional nanowire-like morphological boron-doped diamond grains with sp^2-graphitic phases at the grain boundaries. A high electrical conductivity and superior plasma illumination (PI) characteristics, viz. low breakdown voltage and longer lifetime stability were achieved for the nanowire morphological NCD films. For the purpose of understanding the origin of nanowires and graphitic phases at the grain boundaries ensuing in high value of electrical conductivity and superior PI characteristics, the role of boron, nitrogen and *T*s in modifying the constituents in

the plasma leading to the microstructural modification of NCD thin films is systematically explored. To the best of our knowledge, the collective effect of boron, nitrogen and *T*s for the evolution of microstructure, electrical conductivity and PI characteristics of diamond films is not described yet.

■ EXPERIMENTAL METHODS

A MWPECVD (SEKI Technotron AX5400S, Japan) system was utilized to deposit the NB-NCD films on highly resistive (100) silicon substrates ($1 \times 1\ cm^2$). Preparation of the substrate consisted of: washing for 5 minutes. first in acetone then in isopropanol in an ultrasonic bath. Then the substrates were sonicated in nanodiamond suspension (BlueSeeds, Adámas Nanotechnologies, USA) for 30 min.[20] The following parameters were used to create NB-NCD films: gas mixture H_2: CH_4: B_2H_6: N_2 ratio with a total flow rate of 328 sccm (the B_2H_6 was used at 2000 ppm of [B] / [C] ratio an acceptor precursor); microwave power of 1300 W (2.45 GHz); pressure of 6.7×10^3 Pa; growth time of 60 min; and substrate temperatures (*T*s) ranging from 400 to 850 °C. The temperature *T*s was controlled by a thermocouple placed in an induction heated table. The temperature set on the heated stage was measured with a thermocouple and stabilized with a PID controller. Additionally, the temperature of samples was monitored utilizing a dual wavelength pyrometer (Williamson Model 90). Nevertheless, the pyrometer readout is hampered with a large inaccuracy caused by the variation of the emissivity coefficient of the samples during the growth and layer formation. Since the thermocouple is the only source of stable and reliable temperature value set and stabilized during the CVD process, we have listed those values as representative experimental parameters.

Field emission scanning electron microscopy (FESEM) via a Hitachi-SU8010 scanning electron microscope, using a 15 kV beam accelerating voltage working in high vacuum mode was utilized to observe the morphology of the NB-NCD films' surfaces. The

Raman spectra were acquired using a visible-Raman spectrometer with 632 nm excitation wavelength and a 325 nm UV light spectrophotometer on the Horiba Jobin Yvon LabRam HR 800 UV to characterize the bonding structures of NB-NCD films. High-resolution X-ray photoelectron spectroscopy (XPS) studies were carried out to evaluate the alteration of the surface chemistry of the samples grown using different *T*s, using Escalab 250Xi spectroscope (ThermoFisher Scientific, USA).[20] Furthermore, the plasma constituents were examined by optical emission spectroscopy (OES) using a 0.3 m monochromator (SR303i, Andor) equipped with 1200 grooves per mm grating and an ICCD detector (DH740, Andor). The OES-spectrometer was calibrated with Calibration Light Source CAL-2000 (Ocean Optics, US).

Using four-point probe technique, the electrical resistivity of the NB-NCD films was evaluated at various measurement temperatures (*T*m) by using needle-like probes of radius 20 μm using Python-driven procedure at Keithley 2400 sourcemeter. Hall effect measurements by using van der Pauw configuration (ECOPIA HMS-3000) were carried out from room temperature (RT) to 573 K in a magnetic field of 0.55 T to estimate the electrical conductivity, mobility and carrier density of the films.

The plasma illumination characteristics were investigated using a microcavity, wherein anode was an indium tin oxide (ITO)-coated glass and cathode was diamond films. A Teflon spacer of thickness 1.0 mm was utilized to separate cathode and anode. A 8.0 mm diameter circular hole was made from the Teflon spacer to form a microcavity. The plasma was triggered in bipolar pulse mode with the help of a pulsed DC voltage at a Ar gas pressure of 1.3×10^4 Pa. An USB microscope was utilized to view the plasma. Using a Keithley 2470 electrometer, the current versus voltage characteristics were estimated.

■ RESULTS AND DISCUSSION

Figures 1a–d show the FESEM micrographs of NB-NCD films grown at various *T*s, which reveal a drastic modification in the morphology of diamond films when *T*s increases from 400–850ºC. At 400ºC, the NB-NCD films possess randomly oriented sharp-edged faceted distinct grains of size ~86 nm (curve I of Figure 1e) with well-defined boundaries. Upon increasing the *T*s to 550ºC and 700ºC, coarsened diamond grains with roundish granular structure are seen in Figures 1b and c. The size of the diamond grains varies from 63 nm to 42 nm while increasing the Ts from 550ºC to 700ºC (curve I of Figure 1e). However, for the films grown at 850ºC (Figure 1d), one-dimensional (1D) randomly oriented wire-like structured grains are observed. The length of the nanowires is between 50−180 nm and few nanometers in diameter. From this time, the NB-NCD films with nanowires are denoted as "nitrogen incorporated boron doped nanocrystalline diamond nanowire (NB-DNW) films" in the subsequent sections of this article. Various groups also reported the fabrication of one-dimensional nanostructures from diamond thin films, which involves multi-steps and complicated processes,[21] whereas the fabrication of NB-DNW films involves a single step growth process.

From the cross-sectional FESEM micrographs (insets of Figures 1a–d), the growth rate of these films (curve II of Figure 1e) was estimated. The growth rate of these films increases from ~546 nm/h to ~972 nm/h when *T*s increases from 400ºC to 700ºC. However, the growth rate suddenly decreases to ~552 nm/h for the NB-DNW films. Previous reports[22] stated that the reduction of growth rate is because of the occurrence of more active CN species at high *T*s. The evolution of the microstructure of these films grown at various *T*s will be discussed in detail shortly.

Besides FESEM, non-contact atomic force microscopy (AFM) measurements were also carried out in order to estimate out the surface roughness of the films. Figures 2 a_I–d_I show the two-dimensional surface features of the NB-NCD films grown at various *T*s. The

surface roughness of polycrystalline diamond films is governed by growth chemistry, grain orientation, and thickness of the films. The value of surface roughness with respect to the *T*s is shown in curve III of Figure 1e, which depicts that roughness value decreased from 14.9 to 8.6 nm with the increase in *T*s up to 700ºC, which is on account of the shrinkage in the grain size and morphological variation of the films (curve I of Figure 1e). But the roughness value increases to about 15.3 nm for the NB-DNW films because of the origin of nanowire-like morphological grains.

Furthermore, the electrical resistivity of the NB-NCD films was measured by using four-point probe technique. The resistivity values show a downward trend with increase in *T*s (Figure 3a). The resistivity values of 1.5×10^{8} Ω cm, 2.5×10^{5} Ω cm and 2.0×10^{2} Ω cm were observed for the films grown at 400ºC, 550ºC and 700ºC, respectively. Remarkably, the NB-DNW films display the lowest resistivity of 9.0×10^{1} Ω cm, leads to high electrical conductivity.

Figure 4a displays the room temperature (RT) electrical conductivity (σ) and mobility (μ) values of NB-NCD films estimated by the Hall measurement system in the van der Pauw configuration. The Hall coefficients with positive value indicates that holes are the majority charge carriers of NB-NCD films. The σ values of the NB-NCD films carried out at room temperature increase monotonically with increasing *T*s (curve I, Figure 4a) and interestingly NB-DNW films show the highest σ value of 8.6×10^{-3} 1/(Ohm•cm) with a carrier density (n) of 2.7×10^{18} /cm^3, respectively. On the other hand, the μ values follow a downward trend as shown in curve II, Figure 4a and reaches the lowest mobility of 0.97 cm^2/V•s for NB-DNW films. Here σ, n and μ values vary with *T*s for NB-NCD films is given in Table 1.

In addition, the Hall measurements were carried out at different *T*m ranging from RT to 573 K (Figure 3b). All the films show increasing trend for σ (Figure 3b) and n (Figure 3c) and decreasing trend in μ (Figure 3d) with an increase in *T*m. The NB-DNW films show the

highest σ value of 1.05 1/(Ohm•cm) with n of 9.5 × 10^{19} /cm^3 at Tm=573 K. The increase in the electrical conductivity with Tm, thus revealing a thermally activated conduction mechanism.[23] Moreover, the decrease in mobility of these films with respect to Ts and Tm is because of the neutral impurity scattering.[24,25]

The activation energy (E_a) of NB-NCD films was estimated by using the equation given in reference 26. The E_a values decreased from 0.35 to 0.25 eV with increasing Ts (curve I, Figure 4b). The decrease in E_a values with an increase in carrier density values can be clarified with regard to impurity band conduction.[27] The compensation ratio (k) of these films was also calculated (curve II, Figure 4b) and the k values were increased while increasing the Ts. As the compensation ratio is related to the total number of ionized impurities present in the NB-NCD films, the mobility decreases when the compensation ratio increases.[28]

From the microscopic perspective, the conductive AFM (C-AFM) measurements were performed to observe the key current conducting paths of these films. The emission current images in Figures 2a_{II}–d_{II} demonstrate the mapping of localized field emission current attained under 5 V sample bias voltage in agreement with the AFM topographic images shown in Figures 2a_I–d_I, respectively. The brighter regions in the emission current images of films signify larger emission current. The grain boundaries show larger emission current as compared to the grains. Particularly, the NB-DNW films illustrate high emission sites in contrast with other NB-NCD films. Also, the grains of NB-DNW films emit significantly due to easy transport of electrons to the grains of these films. Conversely, the NB-NCD films grown at 400ºC show less emission sites because of the presence of sharp-edged faceted grains.

Such observation was validated by the current profiles (insets of Figures 2a_{II}–d_{II}) taken from the emission current images of corresponding NB-NCD films shown in Figures

$2a_{II}$–d_{II}, respectively. The NB-DNW films show the highest peak current of 3.7 nA (Figure $2d_{II}$), whereas the NCD films grown at 400ºC shows the lowest peak current of 1.7 nA (Figure $2a_{II}$). Moreover, the NB-DNW films possess larger number density of highly conductive regions from both grains and grain boundaries, ensuing in the generation of current conduction nanochannels, which leads to the highest electrical conductivity of the NB-DNW films (Figure 3). Such high electrically conducting diamond films are commendable for the fabrication of electron emitting devices such as microplasma illumination devices.

The NB-NCD films were applied as cathodes for the microplasma device and NB-DNW films show improved PI characteristics. Figure 5a shows the measurement setup of microplasma illumination device. The photographs displayed in Figure 5b demonstrate the PI characteristics of the NB-NCD films utilized as cathodes in the microplasma illumination device. Comparatively the NB-DNW films as cathode triggered the plasma at the lowest voltage of 330 V from other NB-NCD films as cathodes in the microplasma device (Figure 5b I–III),. With increase in applied voltage, the brightness of the PI increases. The graph between plasma current density (J_{pl}) and applied field (E) illustrated in Figure 5c display a deviation in the threshold field (E_{th}) with increase in *T*s. The NB-DNW films showed the lowest E_{th} value of 3300 V/cm and the highest J_{pl} value of 1.04 mA/cm^2 at E = 5200 V/cm. It is clearly evident that a material with high electrical conductivity performs well as a cathode in the microplasma devices. Furthermore, the plasma lifetime stability of the NB-NCD films is examined at a constant J_{pl} of 0.6 mA/cm^2 (inset of Figure 5c). The NB-DNW films acquire the highest plasma lifetime stability of 520 min as associated to the other NB-NCD films utilized as cathodes in the microplasma devices. Interestingly, the PI performance of the NB-DNWs displays substantial improvements as compared to other materials as cathodes in the microplasma device reported earlier (Table 2).[29–41]

Now the question arising that: what is/are the key factor(s) accountable for high emission sites from both grains and grain boundaries prominent to superior electrical conductivity and improved plasma illumination characteristics of NB-DNW films? To identify the answers, the bonding characteristics and the microstructure of these NB-NCD films were thoroughly examined using Raman, XPS and TEM with EELS. Raman spectroscopy is a significant tool to investigate the carbon phases existing in the NB-NCD films synthesized as a function of *T*s. Figure 6a displays the UV-Raman spectra (λ=325 nm) of the NCD films. A sharp Raman peak at 1334 cm^{-1} ("dia") for the NB-NCD films grown at 400ºC (spectrum I, Figure 6a) indicates the bigger grain size of diamond for these materials (cf. Figure 1a). The ν-band appeared at ~1160 cm^{-1} represents the existence of *trans*-polyacetylene (*t*-PA) phases of C–H and C=C bonds.[42] The peak at 1360 cm^{-1} (designated as D-band) corresponds to the disordered carbon and the peak at 1580 cm^{-1} (named as G-band) corresponds to the ordered sp^2-bonded carbon present in the NB-NCD films.[43] The shrinking of the diamond peak at 1334 cm^{-1} and the broadening of other Raman peaks with increase in the *T*s (550ºC and 700ºC) (spectra II and III, Figure 6a) indicates the formation of nanocrystalline features in these films, viz. reduction in grain size and increase of grain boundaries. At *T*s=850ºC, the diamond peak is hardly visible, the ν band vanished and the G-band significantly narrowed that indicate NB-DNW films comprise of more sp^2-bonded carbon phases.

Furthermore, by measuring the full-width half maximum (FWHM) of the diamond peak and the non-diamond peak, i.e., ratio of sp^3 to sp^2 content (f_q), was calculated by using equation (1),

$$f_q = \frac{75I_d}{75I_d + \sum_{nd} I_{nd}} \times 100 \qquad (1)$$

where I_d = area under the diamond peak, I_{nd} = area under the non-diamond peak and 75 = signal efficiency factor.[44] As observed from curve II of Figure 6b, the f_q decreases when the *T*s increases, indicating a transformation from sp^3 to sp^2 in these NB-NCD films while increasing the *T*s.

On the other hand, the crystallite size (L_a) of these NB-NCD films was also calculated using equation (2)[45]

$$L_a = \frac{560}{E_l^4}\left(\frac{I_D}{I_G}\right)^{-1} \qquad (2)$$

From curve II of Figure 6b, it is observed that L_a decrease with increase in *T*s up to 700ºC and then it starts increasing for NB-NCD films grown at 850ºC, which supports the findings in SEM morphology (Figure 1).

To validate the formation of sp^2-graphitic phases in these NB-NCD films, visible-Raman spectroscopy measurements were carried out because visible-Raman spectroscopy of λ = 632 nm is highly responsive to sp^2-bonded carbon materials. Figure 7a displays the visible-Raman spectra of the NB-NCD films. The peak at 1334 cm^{-1} representing to sp^3-bonded carbon (diamond) is observed only for the NB-NCD films grown at 400ºC (spectrum I, Figure 7a) and not sharp as observed from UV-Raman spectroscopy (cf. Figure 6a). When *T*s increases, the diamond peak coincides by the D band around 1360 cm^{-1} (spectra II–IV, Figure 7a). Moreover, the FWHM of G band is found to decrease (curve I, Figure 7b) and the position of G band is shifted to a higher wavenumber (curve II, Figure 7b) with increase in *T*s. These phenomena can be realized with regard to tighter-bonding angle and bonding length distributions[46] and the formation of sp^2-graphitic content in the films as the *T*s increases. A similar decrease in sp^3 content was observed by Marchon *et al.*[47]

In addition, curve I of Figure 7c shows an increase in I_D/I_G ratio (ratios of the integrated intensities of the D and G lines) with respect to *T*s, which is due to the weakening of disorder in the bonding angle and/or the evolution of the sp^2-graphite structure in the films.[48] Moreover, curve II of Figure 7c shows a decrease in $I_{t\text{-}PA}/(I_D + I_G)$ ratio of the films with respect to *T*s, indicating a reduction in the *t*-PA content with increase in *T*s as compared to the other sp^2 bonded graphitic phases in the films.[22] From these observations it is evident that *T*s plays a major role for the formation of sp^2 bonded graphite in the films grown at higher *T*s. A TEM-EELS study was done to support this analysis, which will be discussed shortly.

XPS studies were executed to investigate the chemical bonding characteristics over the surface of NB-NCD films. There are observable differences in the position and geometry of the recorded C1s (Figure 8a), B1s (Figure 8b) and N1s (Figure 8c) spectra, testifying a significant influence of *T*s during the synthesis of NB-NCD films. The deconvolution model for the spectra recorded in the core level C1s binding energy range was composed of four different components. The two primary components, deconvoluted at 284.3 and 285.1 eV, signify sp^2- and sp^3- carbons, respectively.[49] It should be noted that these two might be partially overlapped by the peak at 284.6 eV and originating from the adventitious carbon due to exposure of samples to the atmosphere. The small component negatively shifted at 283.4 eV is characteristic of the C-B bonds,[50] while the peak located around 286.2 eV corresponds to C-O bonds in surface hydroxyl groups and possible C-N interactions. The above-presented deconvolution model was successfully utilized in our previous studies on boron-doped carbon nanowall films.[51] The peak deconvolution results are tabulated in Table S1.

The most notable feature observable within the C1s spectra is the shift towards low binding energies, which is the effect of the increasing share of sp^2-carbon species with the increasing *T*s maintained for sample growth. The sp^2-to-sp^3 ratio calculated based on the XPS

C1s peak deconvolution raises from 0.15:1 up to 5.0:1 at the highest *T*s of 850ºC. The higher the *T*s the more evident is the formation of bonds between carbon and boron atoms (C1s C-B share: 1.3 at.% at 400ºC, 4.0 at.% at 850ºC), which is a testimony for the decreased C-sp^3 share, the increased sample conductivity and corroborate Raman spectroscopy findings. On the other hand, the appearance of surface hydroxyl groups does not change significantly between studied samples. The core level B1s binding energy spectra were deconvoluted with the model composed of two-to-three components. The spectra composed of two partially overlapping peaks, at 186.1 and 187.9 eV, and corresponding to elemental boron and B-C bonds. However, the broadening of the spectrum recorded for the sample grown at the highest *T*s indicates the presence of additional component identified as B-O interaction.[52]

The structural modification of the studied samples has its source in boron and nitrogen incorporation in the boron-doped carbon nanowall crystal lattice.[20] While the amount of total boron identified in the samples only marginally rises with the *T*s. It should be noted that boron incorporated in the substrate lattice grows over 2 times (B1s B-C share: 0.2 at.% at 400ºC, 0.5 at.% at 850ºC). The growth carried out at 850ºC consequences in notable oxidation of the incorporated boron species, negligible at lower process temperatures. Moreover, the nitrogen incorporation in the crystal lattice is also observed for samples grown at temperatures exceeding 550ºC, as testified by the N1s peak located at 399.5 eV, characteristic of C-N bonds. Its presence at lower temperatures is plausible, yet below the threshold of the spectroscope (0.1 at.%).

From Raman and XPS studies, it is observed that NB-DNW films grown at 850ºC possess more sp^2-graphitic phases along with the sp^3-diamond. To investigate in detail, the microstructure of NB-DNW films was studied by TEM. Figure 9a illustrates a typical bright field TEM (BF-TEM) micrograph of the NB-DNW films that signifies the origin of one-dimensional wire-like nanostructure. The branching features at the nanowires represent the

occurrence of an anisotropic grain growth in NB-DNW films. The inset of Figure 9a illustrates the selective area electron diffraction (SAED) pattern of the BF-TEM micrograph revealed in Figure 9a. The SAED pattern comprises of (111), (220), and (311) diffraction rings, which signifies the diamond lattice and a diffuse ring at the center of the SAED pattern denotes the existence of sp^2-bonded carbon in this film. Moreover, Figure 9b displays the the merged dark field TEM (mDF-TEM) image of NB-DNW films, which is attained by superimposing several diffraction spots of the SAED pattern (inset of Figure 9a). The formation of wire-like diamond grain (yellow regions) in conjunction with graphitic phases (green regions) surrounding the diamond grains are clearly observed from mDF-TEM images. Furthermore, the high resolution TEM (HRTEM) micrograph of NB-DNW films, in relation to the region "A" in Figure 9a, is shown in Figure 9c. The Fourier transformed (FT_0) diffractogram image shown in the inset of Figure 9c contains diamond core in this cluster, which is confirmed from the presence of faint diffraction spots (designated as D) and a strong central diffuse ring with a donut appearance (designated as G) specifies the presence of sp^2-graphitic phases in the NB-DNW films. Moreover, the FT diffractogram images (FT_1-FT_3) taken from regions 1–3 of Figure 9c symbolize the existence of diamond and graphite in the NB-DNW films.

To explore the various carbon phases present in NB-DNW films, we carried out the carbon K-edge EELS in TEM. Figure 9d depicts the core-loss EELS spectrum of the NB-DNW films. A significant rise of peak at 289 eV (σ*-band) and a dip for the energy of 302 eV (second diamond phase) indicates the presence of sp^3-bonded carbon (i.e., diamond) and a π*-band at 285 eV indicates the occrance of sp^2-bonded carbon in the NB-DNW films.[53] To categorize between amorphous carbon and graphite phases, the plasmon-loss EELS measurements in TEM were also executed. The plasmon-loss EELS spectrum of the NB-DNW films revealed in Figure 9e reveals a peak nearby 33 eV (S_4) together with a shoulder

peak near to 23 eV (S_2) designate diamond phases and another peak about 27 eV (S_3) authorises the graphitic phase in the NB-DNW films.[54] It is obvious from the TEM and EELS investigations that the NB-DNW films comprise a hybrid structure of wire-like diamond grains with well-crystallized graphitic grain boundary phases, which support the findings from Raman and XPS studies.

It is reported that conduction of electrons from diamond films instigates favourably from the grain boundaries and not from the topographical structures.[55] But this observation was noticed for low-doping diamond films wherein grain boundaries are electrically conducting as related to the bulk grains. Hence, the electrons transport easily through the grain boundaries from the base to the surface of the film and then ejected. But the condition changes when the grain is electrically conducting, initiating the transportation of electrons through the grain itself and emitted. From C-AFM studies (cf. Figure 2), it is evident that the NB-DNW films possess higher number density of conductive regions than those of other samples. According to the TEM-EELS, XPS and Raman studies, the NB-DNW films contain high sp^2-bonded graphitic phases at the boundaries of each diamond grains, which results into high emission sites. In addition, because of direct doping of boron in diamond lattice,[56] the diamond grains become electrically conducting resulting in more emission sites of NB-DNW films (cf. Figure 2d_{II}). The presence of high density localized electron emission sites indicates the realization of electrically conducting nanochannels at the nanowire-like boron doped diamond grains along with the induction of graphitic grain boundaries, ensuing a high electrical conductivity and improved PI characteristics of NB-DNW films.

It should be revealed that by the application of high voltage, i.e., 450 V, the lifetime PI measurement was carried out, which is shown in the inset of Figure 5c. During measurement, Ar ions were continuously bombarding the cathode material with a high kinetic energy of 450 eV, hence a high erosion rate might experience by the cathode materials. In

real applications, in order to decrease the kinetic energy of Ar ions that bombard the cathode, one possibility is to lower the cathode-to-anode voltage (e.g. <200 V), which will increase the lifetime of the cathode material. Nevertheless, the lifetime will be too long to be computable in a sensible timescale for NB-DNW films. To comprehend the probable mechanism, it is required to address the plasma process of a microplasma device. Along with Ar species, the plasma typically comprises of ample ions and electrons. Because of the continuous bombardment of these mentioned charged particles with anodes and cathodes as well as on the walls of the container, the plasma loses the electrons and ions. Hence, it requires an endless refill of electron–ion pairs and carried out usually by complenting secondary electrons, which are released from the cathode. These secondary electrons are speeded by the bias voltage and consequently generate new electron–ion pairs due to the ionization of the plasma species (Ar). As diamond possess large secondary electron emission co-efficient, therefore it is preferred as a cathode material for the microplasma device. Even tens of micron thick plasma sheath were produced close to the cathode in a plasma, which improved immediately the electric field experienced by the cathode, but still such a field is not large adequate to instigate the electron emission process for the NB-DNW films. The more probable factors responsible for the increase in the secondary electron emission coefficient are the conducting diamond grains and graphitic phases of NB-DNW films. But the cause for the enhancement in secondary electron emission coefficient for NB-DNW films owing to conducting diamond grains and graphitic grain boundary phases is still not fully understood yet.

From the characterization studies, it is evident that the one-dimensional nanowire-like boron doped diamond grains along with the graphitic phases in the NB-DNW films are the key factors for the improvement in the electrical conductivity, leading to the superior microplasma illumination characteristics. However, the role of substrate temperature, boron

doping and nitrogen incorporation on the microstructural evolution of the NB-NCD films is unknown. Particularly, the origin of one-dimensional diamond nanowires along with the graphitic phases, grown using $H_2/CH_4/B_2H_6/N_2$ remains unidentified. The constituents of the plasma were proofed using *in situ* OES measurements to derive the growth mechanism (Figure 10). Figure 10a illustrates the optical emission spectra obtained from plasma during the growth of NB-NCD films from $H_2/CH_4/B_2H_6/N_2$ gas mixtures with changing the *T*s. The Balmer atomic hydrogen emission lines, i.e., the H_α and H_β lines are observed at ~655 and ~484,[57] respectively. The incorporation of nitrogen is evidenced from the CN violet system at 387.3 nm and 418.1 nm and the N_2 peak at 357.3 nm.[58] The CH species at 430 nm and the C_2 swan system between ~472 nm and ~516 nm are observed.[59] The presence of boron is confirmed from the presence of BH band at 433 nm, which confirms that the diamond grains are doped with boron. Furthermore, Figure 10b displays the change in the ratios of CN, C_2, CH, N_2, and NH emission intensities to H_β emission intensity in the plasma. It is obvious that the CN/H_β ratio increases abruptly from 0.65 to 1.2 when *T*s increases from 400°C to 850°C, which indicates CN species show a crucial role in the evolution of microstructure of these NCD films.

Literature reports that the CH_3 species in CH_4/H_2 plasma (excluding B_2H_6 and N_2) are the major species accountable for the formation of diamond grains with micron-size in the MCD films.[60] Though, CH_3 species are not noticeable in this OES spectrum.[61] The same growth mechanism for the synthesis of MCD films is applicable for the NB-NCD films grown at 400°C, nevertheless the plasma containing C_2 and CH species significantly reduces the grain size of the films. It is to be noted that the CN species at low *T*s (400°C) do not play any role in the growth of micron-sized grains as they need high *T*s (700°C) to achieve high activation energy.[62]

When *T*s increases to 550°C and 700°C, the C_2 and CH(CN) species play their role by re-nucleating in the synthesis of nano-sized roundish granular coarsened diamond grains of NB-NCD films. This observation is well associated with the growth of ultrananocrystalline diamond film in CH_4/Ar or CH_4/N_2 gas mixtures,[63] in which the re-nucleation of diamond is done by the C_2-species effortlessly,[64] while the CH(CN) species passivate the diamond nuclei effectively and ensuing in equi-axed ultra-small nanocrystalline diamond grains for the NB-NCD films grown at 550°C and 700°C, respectively.[65]

Theoretically it is disclosed that the CN species preferentially stick to the distinct faces (for example (100) faces) of the nanodiamonds and persuade the origin of one-dimensional nanostructured diamond grains.[66] The surface of the C_2 dimers were adhered by CN species that induces an anisotropic growth of diamond in [100] direction because the energetically favourable CN molecule remains over the growth surface.[67] Experimental studies also evidenced the conversion of equi-axed granular structure to wire-like structure due to the occurrence of abundant CN species at or above the *T*s of 700°C.[67] From the above-obtained results, it is evident that the CN species possess high activation energy than CH species and hence CN species attached to C_2 species leading to the growth of diamond grains in an anisotropic manner. Consequently, the CN species are important for the formation of nanowire-like diamond grains in the NB-DNW films at *T*s=850°C.

Therefore, in NB-DNW films the smaller grains merge along any required direction, resulting in the formation of one dimensional diamond nanowires with high aspect ratio. Furthermore, during this anisotropic growth of diamond nanowire, the surface graphitic carbon atoms encapsulating the sp^3-bonded diamond core are energetically favourable that lead to the formation of sp^2-bonded carbon. Specifically, it is typical on the formation of graphitic layers encircling the diamond grains throughout this anisotropic growth. Hence from OES studies, it is authorized that CN and C_2 species are playing the key roles on the

origin of diamond nanowires and the formation of graphitic phases at the grain boundaries of NB-DNW films. The hybrid structure comprising nanowire-like boron doped diamond grains and graphitic grain boundary phases facilitates an easy transport of electrons, rendering NB-DNW films to show high electrical conductivity and advanced PI characteristics.

■ CONCLUSIONS

Nitrogen incorporated boron doped nanocrystalline diamond (NB-NCD) films are grown using $H_2/CH_4/B_2H_6/N_2$-based microwave plasma enhanced chemical vapour deposition system. The effect of substrate temperature on various characteristics of the films is deliberated. Field emission scanning electron microscopy reveals that, while the *T*s at 400°C ensued in micron-sized diamond grains, increasing the substrate temperature reduces the grain size, resulting in nano-sized diamond grains for the NB-NCD films grown at 550°C and 700°C. Interestingly, when the substrate temperature rises to 850°C, it enables the origin of nanowire-like morphological NB-NCD films. Moreover, the existence of boron and nitrogen in the NB-NCD films is observed by C1s X-ray photoelectron spectroscopy. The Raman spectroscopy and the transmission electron microscopy-electron energy loss spectroscopy evidence the co-existence of sp^3-diamond and sp^2-graphite in the NB-NCD films. The microstructural investigation, accomplished with the help of high-resolution TEM with EELS, indicates that the graphitic phases are existing in the grain boundaries of diamond grains of nanowire-like NB-NCD films. The electrical conductivity studies confirms that the NB-NCD films grown at 850°C (NB-DNWs) are the most electrically conducting, with conduction mediated through the conducting diamond grains (due to boron doping) and the graphitic phases at the grain boundaries (due to nitrogen incorporation). The conducting atomic force microscopy studies also show emission sites originate both from the grains and also from the grain boundaries. These one-dimensional NB-DNW films show superior plasma illumination characteristics viz. low breakdown voltage, high plasma emission current

density and long lasting plasma stability. The optical emission spectroscopy investigation confirms that active CN, C_2, and BH species at higher substrate temperature are the key factors for the origin of nanowire-like conducting diamond grains with graphitic grain boundaries. This novel featured one-dimensional nanowire-like NB-NCD films evidence a high effectiveness in plasma illumination that bring a pathway to the future microplasma devices and related applications.

■ ASSOCIATED CONTENT

Supporting Information

The Supporting Information is available free of charge at

Chemical Composition (in at.%) of NB-NCD films Grown using Different Substrate Temperatures 400°C, 550°C, 700°C and 850°C in $H_2/CH_4/B_2H_6/N_2$ Plasmas, based on the high-resolution XPS studies with proposed deconvolution model (Table S1).

■ AUTHOR INFORMATION

Corresponding Authors

Kamatchi Jothiramalingam Sankaran-*CSIR-Institute of Minerals and Materials Technology, Bhubaneswar 751013, India;*

E-mail: kjsankaran@immt.res.in

Robert Bogdanowicz-*Department of Metrology and Optoelectronics, Faculty of Electronics, Telecommunications and Informatics, Gdansk University of Technology, 80-233 Gdansk, Poland;*

E-mail: rbogdan@eti.pg.edu.pl

Authors

Salila Kumar Sethy-*CSIR-Institute of Minerals and Materials Technology, Bhubaneswar 751013, India*

Mateusz Ficek-*Department of Metrology and Optoelectronics, Faculty of Electronics, Telecommunications and Informatics, Gdansk University of Technology, 80-233 Gdansk, Poland*

Sourav Sain-*Department of Physics, School of Natural Sciences, Shiv Nadar University, Gautam Buddha Nagar, Uttar Pradesh 201314, India*

Anupam Ruturaj Tripathy- *Institute of NanoEngineering and MicroSystems, National Tsing Hua University, Hsinchu 30013, Taiwan, Republic of China*

Shivam Gupta-*Department of Materials Science and Engineering, National Tsing Hua University, Hsinchu 30013, Taiwan, Republic of China*

Jacek Ryl-*Department of Electrochemistry, Corrosion and Materials Engineering, Faculty of Chemistry, Gdansk University of Technology, 80-233 Gdansk, Poland*

Susanta Sinha Roy-*Department of Physics, School of Natural Sciences, Shiv Nadar University, Gautam Buddha Nagar, Uttar Pradesh 201314, India*

Nyan-Hwa Tai-*Department of Materials Science and Engineering, National Tsing Hua University, Hsinchu 30013, Taiwan, Republic of China*

Complete contact information is available at:

https://pubs.acs.org/10.1021/acsami.1c05542

Author Contributions

†S.K.S and M.F. are first authors.

Notes

The authors declare no competing financial interest.

■ ACKNOWLEDGEMENTS

The authors like to thank the financial support of the Council of Scientific and Industrial Research, India via Research Grant OLP-106 and the Science and Engineering Research Board, India via Research Grant GAP-336.

■ REFERENCES

(1) Verma, R.; Adhikary, R. R.; Banerjee R. Smart Material Platforms for Miniaturized Devices: Implications in Disease Models and Diagnostics. *Lab Chip.* **2016**, *16*, 1978–1992.

(2) Rajwar, A.; Kharbanda, S.; Chandrasekaran, A. R.; Gupta, S.; Bhatia D. Designer, Programmable 3D DNA Nanodevices to Probe Biological Systems. *ACS Appl. Bio Mater.* **2020**, *3*, 7265−7277.

(3) Chiang, W. H.; Mariotti, D.; Sankaran, R. M.; Eden, G.; Ostrikov, K. Microplasmas for Advanced Materials and Devices. *Adv. Mater*. **2020**, *32*, No. 1905508.

(4) Schoenbach, K. H.; Becker, K. 20 years of Microplasma Research: a Status Report. *Eur. Phys. J. D*. **2016**, *70*, No. 29.

(5) Papadakis, A. P.; Rossides, S.; Metaxas, A. C. Microplasmas: A Review. *J. Appl. Phys.* **2011**, *4*, 45−63.

(6) Iza, F.; Kim, G. J.; Lee, S. M.; Lee, J. K.; Walsh, J. L.; Zhang, Y. T. Kong, M. G. Microplasmas: Sources, Particle Kinetics, and Biomedical Applications. *Plasma Process. Polym*. **2008**, *5*, 322–344.

(7) Liu, Q.; Yang, Z.; Wang, Y.; Ding, G. Electrophoretic Carbon Nanotube Field Emission Layer for Plasma Display Panels. *Nano-Micro Lett*. **2012**, *4(4)*, 247−252.

(8) Sankaran, K. J.; Huang, B. R.; Saravanan, A.; Manoharan, D.; Tai, N. H.; Lin, I. N. Heterogranular-Structured Diamond−Gold Nanohybrids: A New Long-Life Electronic Display Cathode. *ACS Appl. Mater. Interfaces*. **2015**, *7*, 27078−27086.

(9) Tachibana, K. Current Status of Microplasma Research. *IEEJ Trans.* **2006**, *1*, 145–155.

(10) Lou, S. C.; Chen, C.; Teng, K. Y.; Tang, C. Y.; Lin, I. N. Synthesis of Diamond Nanotips for Enhancing the Plasma Illumination Characteristics of Capacitive-type Plasma Devices. *J. Vac. Sci. Technol. B* **2013**, *31*, No. 02B109.

(11) Kunuku, S.; Sankaran, K. J.; Leou, K. C.; Lin, I. N. Microplasma Device Architectures with Various Diamond Nanostructures. *Mater. Res. Express*. **2017**, *4*, No. 025001.

(12) Pakpour-Tabrizi, A. C.; Schenk, A. K.; A. J. U.; Mahatha, S. K.; Arnold, F.; Bianchi, M.; Jackman, R. B.; Butler, J. E.; Vikharev, A.; Miwa, J. A.; Hofmann, P.; Cooil, S. P.; Wells, J. W.; Mazzola, F. The Occupied Electronic Structure of Ultrathin Boron Doped Diamond. *Nanoscale Adv*. **2020**, *2*, 1358–1364.

(13) Lloret, F.; Desta, D.; Rouzbahani, Sankaran, K. J.; Millan-Barba, J.; Gutierrez, M.; Boyen, H. G.; R.; Pobedinskas, P.; Haenen, K. Improved Field Electron Emission Properties of Phosphorus and Nitrogen Co-Doped Nanocrystalline Diamond Films. *Nanomaterials.* **2020**, *10*, No. 1024.

(14) Sankaran, K. J.; Joseph, P. T.; chen, H. C.; Tai, N. H.; Lin, I. N. Investigation in the Role of Hydrogen on the Properties of Diamond Films Grown using $Ar/H_2/CH_4$ Microwave Plasma. *Diamond Relat. Mater.* **2011**, *20*, 232–237.

(15) Bhattacharyya, S.; Auciello, O.; Birrell, J.; Carlisle, J. A.; Curtiss, L. A.; Goyette, A. N.; Gruen, D. M.; Krauss, A. R.; Schlueter, J.; Sumant, A. Synthesis and Characterization of Highly-Conducting Nitrogen Doped Ultrananocrystalline Diamond Films. *Appl. Phys. Lett*. **2001**, *79*, No. 1441.

(16) Sankaran, K. J.; Tai, N. H.; Lin, I. N.; Yeh, C. J.; Pobedinskas, P.;

Hsieh, P. Y.; Kunuku, S.; Leou, K. C.; Haenen, K. Origin of Conductive Nanocrystalline Diamond Nanoneedles for Optoelectronic Applications. *ACS Appl. Mater. Interfaces*. **2019**, *11*, 25388–25398.

(17) Srikanth, V. V. S. S.; Kumar, S.; Kumar, V. B. A Brief Review on the In Situ Synthesis of Boron-Doped Diamond Thin Films. *Int. J. Electrochem. Sci.* **2012**, No. 218393.

(18) Song, C. W.; Cho, D. S.; Lee, J. M.; Song, P. K. Effect of Boron Doping on Diamond Film and Electrochemical Properties of BDD According to Thickness and Morphology. *Coatings* **2020**, *10*, No. 331.

(19) Gajewski, W.; Achatz, P.; Williams, O. A.; Haenen, K.; Bustarret, E.; Stutzmann, M.; Garrido, J. A. Electronic and Optical Properties of Boron-Doped Nanocrystalline Diamond Films. *Phys. Rev. B.* **2009**, *79*, No. 045206.

(20) Bogdanowicz, R.; Sobaszek, M.; Ryl, J.; Gnyba, M.; Ficek, M.; Gołu´nski, Ł.; Bock, W. J.; ´Smietana, M.; Darowicki, K. Improved Surface Coverage of an Optical fibre with Nanocrystalline Diamond by the Application of Dip-Coating Seeding. *Diam. Relat. Mater*. **2015**, *55*, 52–63.

(21) Peng, X.; Chu, J.; Wang, L.; Duan, S.; Feng, P. Boron-Doped Diamond Nanowires for CO Gas Sensing Application. *Sens. Actuators B Chem*. **2017**, *241*, 383–389.

(22) Sankaran, K. J.; Kurian, J.; Chen, H. C.; Dong, C. L.; Lee, C. Y.; Tai, N. H.; Lin, I. N. Origin of a Needle-Like Granular Structure for Ultrananocrystalline Diamond Films Grown in a N_2/CH_4 Plasma. *J. Phys. D: Appl. Phys*. **2012**, *45*, No. 365303.

(23) Gu, S. S.; Hu, X. J. Enhanced P-Type Conduction of B-Doped Nanocrystalline Diamond Films by High Temperature Annealing. *J. Appl. Phys*, **2013**, *114*, No. 023506.

(24) Pernot, J.; Tavares, C.; Gheeraert, E.; Bustarret, E.; Katagiri, M.; Koizumi, S. Hall Electron Mobility in Diamond. *Appl. Phys. Lett.* **2006**, *89*, No. 122111.

(25) Pernot, J.; Volpe, P. N.; Omnès, F.; Muret, P.; Mortet, V.; Haenen, K.; Teraji, T. Hall Hole Mobility in Boron-doped Homoepitaxial Diamond. *Phys. Rev. B.* **2010**, *81*, No. 205203.

(26) Werner, M.; Dorsch, O.; Baerwind, H. U.; Obermeier, E. Charge Transport in Heavily B-doped Polycrystalline Diamond Films. *Appl. Phys. Lett.* **1994**, *64(5)*, 595–597.

(27) Rouzbahani, R.; Nicley, S. S.; Vanpoucke, D. E. P.; Lloret, F.; Pobedinskas, P.; Araujo, D.; Haenen, K. Impact of Methane Concentration on Surface Morphology and Boron

Incorporation of Heavily Boron-doped Single Crystal Diamond Layers. *Carbon* **2021**, *172*, 463–473.

(28) Gabrysch, M.; Majdi, S.; Hallén, A.; Linnarsson, M.; Schöner, A. Twitchen, D.; Isberg, J. Compensation in Boron-Doped CVD Diamond. *phys. stat. sol*. **2008**, *9*, 2190–2194.

(29) Sankaran, K. J.; Srinivasu, K.; Leou, K. C.; Tai, N. H.; Lin, I. N. High Stability Electron Field Emitters Made of Nanocrystalline Diamond Coated Carbon Nanotubes. *Appl. Phys. Lett.* **2013**, *103*, No. 251601.

(30) Sankaran, K. J.; Chang, T. H.; Bikkarolla, S. K.; Roy, S. S.; Papakonstantinou, P.; Drijkoningen, S.; Pobedinskas, P.; Bael, M. K. V.; Tai, N. H.; Lin, I. N.; Haenen, K. Growth, Structural and Plasma Illumination Properties of Nanocrystalline Diamond-Decorated Graphene Nanoflakes. *RSC Adv*., **2016**, *6*, 63178–63184.

(31) Sankaran, K. J.; Afsal, M.; Lou, S. C.; Chen, H. C.; Chen, C.; Lee, C. Y.; Chen, L. J.; Tai, N. H.; Lin, I. N. Electron Field Emission Enhancement of Vertically Aligned Ultrananocrystalline Diamond-Coated ZnO Core–Shell Heterostructured Nanorods. *Small*. **2014**, *10*, 179–185.

(32) Sankaran, K. J.; Ficek, M.; Kunuku, S.; Panda, K.; Yeh, C. J.; Park, J. Y.; Sawczak, M.; Michałowski, P. P.; Leou, K. C.; Bogdanowicz, R.; Lin, I. N.; Haenen, K. Self-organized Multi-layered Graphene-Boron Doped Diamond Hybrid Nanowalls for High-Performance Electron Emission Devices. *Nanoscale*. **2018**, *10*, 1345–1355.

(33) Sankaran, K. J.; Hoang, D. Q.; Korneychuk, S.; Kunuku, S. Thomas, J. P.; Pobedinskas, P.; Drijkoningen, S.; Bael, M. K. V.; D'Haen, J.; Verbeeck, J.; Leou, K. C.; Leung, K. T.; Lin, I. N.; Haenen, K. Hierarchical Hexagonal Boron Nitride Nanowall–Diamond Nanorod Heterostructures with Enhanced Optoelectronic Performance. *RSC Adv*. **2016**, *6*, 90338–90346.

(34) Sankaran, K. J.; Kunuku, S.; Sundaravel, B.; Hsieh, P. Y.; Chen, H. C.; Leou, K. C.; Tai, N. H.; Lin, I. N. Gold Nanoparticle–Ultrananocrystalline Diamond Hybrid Structured Materials for High-Performance Optoelectronic Device Applications. *Nanoscale*, **2015**, *7*, 4377–4385.

(35) Saravanan, A.; Huang, B. R.; Sankaran, K. J.; Tai, N. H.; Lin, I. N. Highly Conductive Diamond−Graphite Nanohybrid Films with Enhanced Electron Field Emission and Microplasma Illumination Properties. *ACS Appl. Mater. Interfaces*. **2015**, *7*, 14035−14042.

(36) Saravanan, A.; Huang, B. R.; Sankaran, K. J.; Kunuku, S.; Dong, C. L.; Leou, K. C.; Tai, N. H.; Lin, I. N. Bias-enhanced Nucleation and Growth Processes for Ultrananocrystalline Diamond Films in Ar/CH_4 Plasma and Their Enhanced Plasma Illumination Properties. *ACS Appl. Mater. Interfaces.* **2014**, *6*, 10566−10575.

(37) Chang, T.; Lou, S.; Chen, H.; Chen, C.; Lee, C.; Tai, N.; Lin, I. Enhancing the Plasma Illumination Behaviour of Microplasma Devices Using Microcrystalline/Ultrananocrystaline Diamond Materials as Cathodes. *Nanoscale*. **2013**, *5*, 7467−7475.

(38) Sankaran, K. J.; Yeh, C. J.; Drijkoningen, S.; Pobedinskas, P.; Van Bael, M. K.; Leou, K. C.; Lin, I. N.; Haenen, K. Enhancement of Plasma Illumination Characteristics of Few-layer Graphene-Diamond Nanorods Hybrid. *Nanotechnology*. **2017**, *28*, 065701.

(39) Deshmukh, S.; Sankaran, K. J.; Srinivasu, K.; Korneychuk, S.; Banerjee, D.; Barman, A.; Bhattacharya, G.; Phase, D. M.; Gupta, M.; Verbeeck, J.; Leou, K. C.; Lin, I. N.; Haenen, K.; Roy, S. S. Local Probing of the Enhanced Field Electron Emission of Vertically Aligned Nitrogen-Doped Diamond Nanorods and Their Plasma Illumination Properties. *Diamond Relat. Mater.* **2018**, *83*, 118−125.

(40) Chang, T. H.; Hsieh, P. Y.; Kunuku, S.; Lou, S. C.; Manoharan, D.; Leou, K. C.; Lin, I. N. ; Tai, N. H. High Stability Electron Field Emitters Synthesized via The Combination of

Carbon Nanotubes and N_2-Plasma Grown Ultrananocrystalline Diamond Films. *ACS Appl. Mater. Interfaces.* **2015**, *7*, 27526–27538.

(41) Sankaran, K. J.; Kicek, M.; Panda, K.; Yeh, C. J.; Sawczak, M.; Ryl, J.; Leou, K. C.; Park, J. Y.; Lin, I. N.; Bogdanowicz, R.; Haenen, K. Boron-Doped Nanocrystalline Diamond−Carbon Nanospike Hybrid Electron Emission Source. *ACS Appl. Mater. Interfaces*. **2019**, *11*, 48612−48623.

(42) Ferrari, A. C.; Robertson, Origin of the 1150-cm^{-1} Raman Mode in Nanocrystalline Diamond. J. *Phys. Rev. B*. **2001**, *63*, No. 121405.

(43) Ferrari, A. C.; Robertson, Interpretation of Raman Spectra of Disordered and Amorphous Carbon. *Phys. Rev. B*. **2000**, *61*, No. 14095.

(44) Shorder, R. E.; Nemanich, R. J.; Glass, J. T. Analysis of the Composite Structures in Diamond Thin Films by Raman Spectroscopy. *Phys. Rev. B*. **1990**, *41(6)*, No. 3738.

(45) Cançado, L. G.; Takai, K.; Enoki, T.; Endo, M.; Kim, Y. A.; Mizusaki, H.; Jorio, A.; Coelho, L. N.; Magalhães-Paniago, R.; Pimenta, M. A. General Equation for the Determination of the Crystallite Size La of Nanographite by Raman Spectroscopy. *Appl. Phys. Lett*. **2006**, *88*, No. 163106.

(46) Tsai, H.; Bogy, D. B. Characterization of Diamondlike Carbon Films and Their Application as Overcoats on Thin-Film Media for Magnetic Recording. *J. Vac. Sci. Technol*. **1987**, *A5*, 3287–3312.

(47) Marchon, B.; Gui, J.; Grannen, K.; Rauch, G. C.; Ager, J. W.; Silva, S. R. P.; Robertson, J. Photoluminescence and Raman Spectroscopy in Hydrogenated Carbon Films**.** *IEEE Trans. Magn*. **1997**, *33(5)*, 3148–3150.

(48) Ferrari, A. C.; Robertson, J. Resonant Raman Spectroscopy of Disordered, Amorphous, and Diamond like Carbon. *Phys. Rev. B*. **2001**, *64*, No. 075414.

(49) Joseph, P. T.; Tai, N.H.; Lee, C. Y.; Niu, H.; Pong, W. F.; Lin, I. N. Field Emission Enhancement in Nitrogen-Ion-Implanted Ultrananocrystalline Diamond Films. *J. Appl. Phys*. **2008**, *103*, No. 043720.

(50) Wang, K.; Kang, X.; Kang, Q.; Zhong, Y.; Hu, C.; Wang, P. Improved Reversible Dehydrogenation of $2LIBH_4$-MgH_2 Composite by the Controlled Formation of Transition Metal Boride. *J. Mater. Chem*. **2014**, *2*, 2146−2151.

(51) Siuzdak, K.; Ficek, M.; Sobaszek, M.; Ryl, J.; Gnyba, M.; Niedziałkowski, P.; Malinowska, N.; Karczewski, J.; Bogdanowicz, R. Boron-Enhanced Growth of Micron-Scale Carbon-Based Nanowalls: A Route Toward High Rates of Electrochemical Biosensing. *ACS Appl. Mater. Interfaces.* **2017**, *9*, 12982−12992.

(52) Kolel-Veetil, M. K.; Gamache, R. M.; Bernstein, N.; Goswami, R.; Qadri, S. B.; Fears, K. P.; Miller, J. B.; Glaser, E. R.; Keller, T. M. Substitution of Silicon Within the Rhombohedral Boron Carbide (B4C) Crystal Lattice Through High-Energy Ball Milling. *J. Mater. Chem. C* **2015**, *3*, 11705−11716.

(53) Prawer, S.; Peng, J. L.; Orwa, J. O.; McCallum, J. C.; Jamieson, D. N.; Bursill, L. A. Size Dependence of Structural Stability in Nanocrystalline Diamond. *Phys. Rev. B: Condens. Matter*. **2000**, *62*, No. R16360.

(54) Kurian, J.; Sankaran, K. J.; Thomas, J. P.; Tai, N. H.; Chen, H.-C.; Lin, I.-N. The Role of Nanographitic Phase on Enhancing the Electron Field Emission Properties of Hybrid Granular Structured Diamond Films: The Electron Energy Loss Spectroscopic Studies. *J. Phys. D: Appl. Phys*. **2014**, *47*, No. 415303.

(55) Harniman, R.L.; Fox, O.J.; Janssen, W.; Drijkoningen, S.; Haenen, K.; May, P.W. Direct Observation of Electron Emission from Grain Boundaries in CVD Diamond by Peak Force-Controlled Tunnelling Atomic Force Microscopy. *Carbon*. **2015**, *94*, 386–395.

(56) Choudhury, S.; Golnak, R.; Schulz, C.; Lieutenant, K.; Tranchant, N.; Arnault, J. C.; Pinault-Thaury, M. A.; Jomard, F.; Knittel, P.; Petit, T. Impact of Nitrogen, Boron and Phosphorus Impurities on the Electronic Structure of Diamond Probed by X-ray Spectroscopies. *C*. **2021**, *7*, No. 28.

(57) Shigesato, Y.; Boekenhauer, R. E.; Sheldon, B. W. Emission Spectroscopy during Direct-Current-Biased, Microwave-Plasma Chemical Vapor Deposition of Diamond. *Appl. Phys. Lett*. **1993**, *63*, 314−316.

(58) Balestrino, G.; Marinelli, M.; Milani, E.; Paoletti, A.; Paroli, P.; Pinter, I.; Tebano, A. Systematic Investigation of Plasma Emission Spectra during Microwave Diamond Deposition from CH_4-CO_2 and C_2H_2-CO_2 Gas Mixtures. *Diamond Relat. Mater*. **1993**, *2*, 389−392.

(59) May, P. W.; Mankelevich, Y. A. From Ultrananocrystalline Diamond to Single Crystal Diamond Growth in Hot Filament and Microwave Plasma-Enhanced CVD Reactors: A Unified Model for Growth Rates and Grain Sizes. *J. Phys. Chem. C*. **2008**, *112*, 12432−12441.

(60) Childs, M. A.; Menningen, K. L.; Chevako, P.; Spellmeyer, N. W.; Anderson, L. W.; Lawler, J. E. Detection of CH_3 During CVD Growth of Diamond by Optical Absorption. *Phys. Lett. A*. **1992**, *171*, 87−89.

(61) Ma, J.; Ashfold, M. N. R.; Mankelevich, Y. A. Validating Optical Emission Spectroscopy as a Diagnostic of Microwave Activated CH_4/Ar/H_2CH_4/Ar/H_2 Plasmas used for Diamond Chemical Vapor Deposition. *J. Appl. Phys*. **2009**, *105*, No. 043302.

(62) Sankaran, K. J.; Lin, Y. F.; Jian, W. B.; Chen, H. C.; Panda, K.; Sundaravel, B.; Dong, C. L.; Tai, N. H.; Lin, I. N. Structural and Electrical Properties of Conducting Diamond Nanowires. *ACS Appl. Mater. Interfaces*. **2013**, *5*, 1294−1301.

(63) Truscott, B. S.; Kelly, M. W.; Potter, K. J.; Ashfold, M. N. R. Microwave Plasma-Activated Chemical Vapor Deposition of Nitrogen-Doped Diamond. II: $CH_4/N_2/H_2$ Plasmas. *J. Phys. Chem. A*. **2016**, *120*, 8537−8549.

(64) Mahoney, E. J. D.; Truscott, B. S.; Ashfold, M. N. R.; Mankelevich, Y. A. Optical Emission from C_2 − Anions in Microwave-Activated CH_4/H_2 Plasmas for Chemical Vapor Deposition of Diamond. *J. Phys. Chem. A*. **2017**, *121*, 2760−2772.

(65) Wang, C. S.; Chen, H. C.; Cheng, H. F.; Lin, I. N. Origin of Platelike Granular Structure for the Ultrananocrystalline Diamond Films Synthesized in H_2-Containing Ar/CH_4 Plasma. *J. Appl. Phys.* **2010**, *107*, No. 034304.

(66) Sternbergt, M.; Zapol, P.; Frauenheimt, T.; Carlisle, J. A.; Gruen, D. M.; Curtiss, L. A. Density Functional based Tight Binding Study of C_2 and CN Deposition on (100) Diamond Surface. *MRS Proc*. **2001**, *675*, W12.

(67) Sankaran, K. J.; Huang, B. R.; Saravanan, A.; Manoharan, D.; Tai, N. H.; Lin, I. N. Nitrogen Incorporated Ultrananocrystalline Diamond Microstructures from Bias-Enhanced Microwave N_2/CH_4-Plasma Chemical Vapor Deposition. *Plasma Process. Polym*. **2016**, *13*, 419−428.

Table 1. Electrical and Microplasma Illumination Characteristics of NB-NCD films Grown using Different Substrate Temperatures 400°C, 550°C, 700°C and 850°C in $H_2/CH_4/B_2H_6/N_2$ Plasmas.

NB-NCD films grown at different substrate temperatures	Hall measurements				Microplasma illumination	
	Resistivity (Ohm•cm)	Electrical conductivity (1/Ohm•cm)	Carrier density ($/cm^3$)	Mobility ($cm^2/V•s$)	Threshold field (V/cm)	Plasma current density (mA/cm^2)
400°C	1.50×10^8	8.7×10^{-5}	1.8×10^{13}	681.7	4500	0.8 @ 600 V
550°C	2.50×10^5	7.5×10^{-5}	6.2×10^{15}	30.7	4000	0.9 @ 580 V
700°C	2.0×10^2	9.1×10^{-4}	7.1×10^{16}	23.9	4000	0.9 @ 560 V
850°C (NB-DNW)	9.0×10^1	8.6×10^{-3}	2.7×10^{18}	0.9	3300	1.04 @ 520 V

Table 2. Plasma Illumination Properties of NB-DNW films compared to Other Cathodic Materials based Microplasma Devices reported in Literature.

Materials	E_{th} (V/μm)	J_{pl} (mA/cm^2)	τ_{pl} (PI lifetime)
Carbon nanotubes[29]	0.32	6.1 @ 0.51 V/μm	190 min
Graphene nanoflakes[30]	0.40	3.3 @ 0.57 V/μm	4 min
Diamond-graphene nanoflakes[30]	0.38	3.8 @ 0.57 V/μm	21 min
Graphite[31]	0.22	2.6 @ 0.35 V/μm	21 min
ZnO nanorods[31]	0.19	3.0 @ 0.30 V/μm	---
UNCD-ZnO nanorods[31]	0.16	3.97 @ 0.30 V/μm	107 min
MLG-BDD hybrid nanowalls[32]	0.33	6.0 @ 0.51 V/μm	358 min
hBN-diamond nanorods[33]	0.35	1.04 @ 0.54 V/μm	29 min
Gold-UNCD hybrids[34]	0.37	3.0 @ 0.52 V/μm	7.12 h
Diamond–graphite nanohybrid films[35]	0.32	2.15 @ 0.51 V/μm	491 min
BEN-BEG UNCD[36]	0.33	1.59 @ 0.57 V/μm	---
MCD-UNCD pyramids[37]	0.20	7.80 @ 0.35 V/μm	133 min
Few-layer graphene-diamond nanorods[38]	0.54	14.80 @ 0.90 V/μm	20 min
Nitrogen doped diamond nanorods[39]	0.39	3.95 @ 0.55 V/μm	433 min
Nitrogen doped diamond films/CNTs[40]	0.36	1.88 @ 0.55 V/μm	218 min
BNCD-CNS hybrids[41]	0.27	16.2 @ 0.50 V/μm	545 min
NB-DNW films[present study]	0.33	1.04 @ 0.52 V/μm	520 min

E_{th}=threshold field; J_{pl}=PI current density; τ_{pl}=PI lifetime

Figure captions

Figure 1. SEM micrographs with the insets showing the cross-sectional SEM micrographs of NB-NCD films grown using different substrate temperatures in $H_2/CH_4/B_2H_6/N_2$ plasmas (a) 400°C, (b) 550°C, (c) 700°C and (d) 850°C. (e) Variation in grain size (curve I), growth rate (curve II) and surface roughness (curve III) of the NB-NCD films with respect to substrate temperatures 400°C, 550°C, 700°C and 850°C.

Figure 2. (a_I–d_I) AFM micrographs and (a_{II}–d_{II}) corresponding C-AFM field emitted current mapping recorded at an applied bias of 5 V of NB-NCD films grown using different substrate temperatures 400°C, 550°C, 700°C and 850°C in $H_2/CH_4/B_2H_6/N_2$ plasmas, respectively. The insets of a_{II}–d_{II} are the corresponding current profiles of C-AFM micrographs shown in figure 2 (a_{II}–d_{II}), respectively.

Figure 3. (a) Four point probe resistivity as a function of measurement temperature for the NB-NCD films grown using different substrate temperatures in $H_2/CH_4/B_2H_6/N_2$ plasmas (I) 400°C, (II) 550°C, (III) 700°C and (IV) 850°C. Hall effect measurements of (b) electrical conductivity, (c) carrier density and (d) mobility as a function of measurement temperatures for the NB-NCD films grown using different substrate temperatures in $H_2/CH_4/B_2H_6/N_2$ plasmas (I) 400°C, (II) 550°C, (III) 700°C and (IV) 850°C, respectively.

Figure 4. (a) The room temperature Hall effect measurements of electrical conductivity (curve I) and mobility (curve II) and (b) the activation energy (curve I) and compensation ratio (curve II) of the NB-NCD films grown using different substrate temperatures 400°C, 550°C, 700°C and 850°C in $H_2/CH_4/B_2H_6/N_2$ plasmas, respectively.

Figure 5. (a) Schematic representation of microplasma illumination device. (b) Plasma illumination characteristics for the microplasma devices utilizing NB-NCD films grown using different substrate temperatures in $H_2/CH_4/B_2H_6/N_2$ plasmas (I) 400°C, (II) 550°C, (III) 700°C and (IV) 850°C as cathodes. (c) Plasma illumination current density (J_{PI}) as a function of applied field (E) of NB-NCD films grown using different substrate temperatures in $H_2/CH_4/B_2H_6/N_2$ plasmas (I) 400°C, (II) 550°C, (III) 700°C and (IV) 850°C. The inset of Figure 5c shows the plasma illumination lifetime stability measurements of NB-NCD films measured at a constant J_{pl} =0.6 mA/cm^2.

Figure 6. (a) UV-Raman spectra (λ=325 nm) of NB-NCD films grown using different substrate temperatures in $H_2/CH_4/B_2H_6/N_2$ plasmas (I) 400°C, (II) 550°C, (III) 700°C and (IV) 850°C. (b) Variation in sp^3/sp^2 content (curve I) and crystallite size (curve II) of the NB-NCD films with respect to substrate temperatures 400°C, 550°C, 700°C and 850°C.

Figure 7. (a) Micro-Raman spectra (λ=632 nm) of NB-NCD films grown using different substrate temperatures in $H_2/CH_4/B_2H_6/N_2$ plasmas (I) 400°C, (II) 550°C, (III) 700°C and (IV) 850°C. (b) Variation in G-band FWHM (curve I) and G-peak position (curve II) of the NCD films with respect to substrate temperatures 400°C, 550°C, 700°C and 850°C. (c) Variation in I_D/I_G (curve I) and $I_{t\text{-}PA}/(I_D+I_G)$ (curve II) of the NB-NCD films with respect to substrate temperatures 400°C, 550°C, 700°C and 850°C.

Figure 8. High-resolution a) C1s, b) B1s, and c) N1s XPS spectra recorded for NB-NCD films grown using different substrate temperatures in $H_2/CH_4/B_2H_6/N_2$ plasmas (I) 400°C, (II) 550°C, (III) 700°C and (IV) 850°C.

Figure 9. (a) Bright field TEM (BF-TEM) micrograph of NB-NCD films grown at 850°C (NB-DNW films) with their corresponding SAED pattern shown as inset and (b) merged dark field TEM image of "a". (c) HRTEM image of region "A" in "a". The insets (FT_0) show the

Fourier-transformed image corresponding to the whole structure image in “c”, whereas the FT_1 to FT_3 images show the FT images corresponding to regions “1 to 3”, respectively. (d) The core-loss and (e) the plasmon loss EELS spectra of NB-DNW films corresponding to BF-TEM image in figure 9(a).

Figure 10. (a) The OES spectra and (b) variation in the C_2/H_β, CH/H_β, N_2/H_β, NH/H_β, and CN/H_β of the corresponding OES spectra of NB-NCD films grown using different substrate temperatures 400°C, 550°C, 700°C and 850°C in $H_2/CH_4/B_2H_6/N_2$ plasmas.

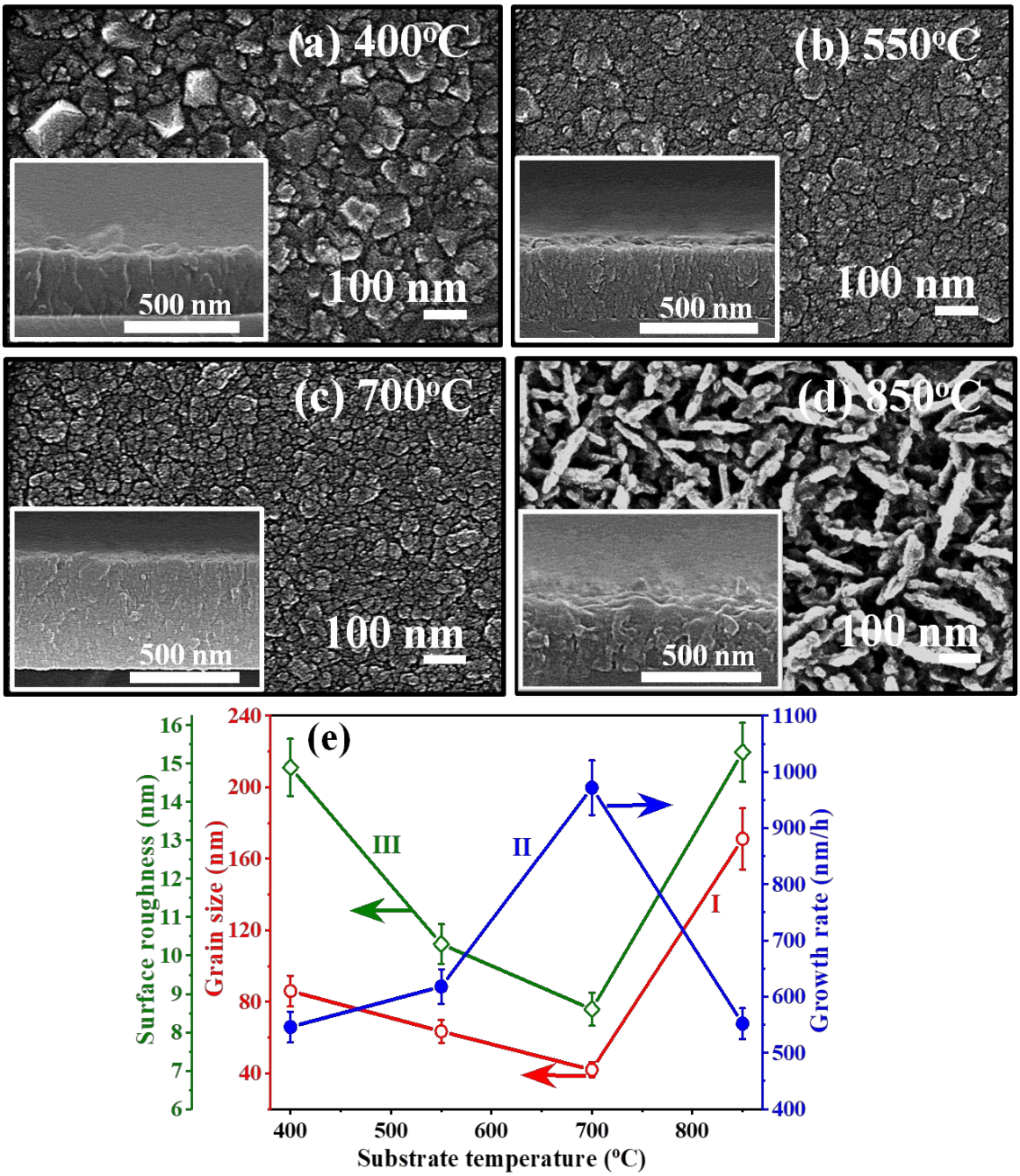

Figure 1.

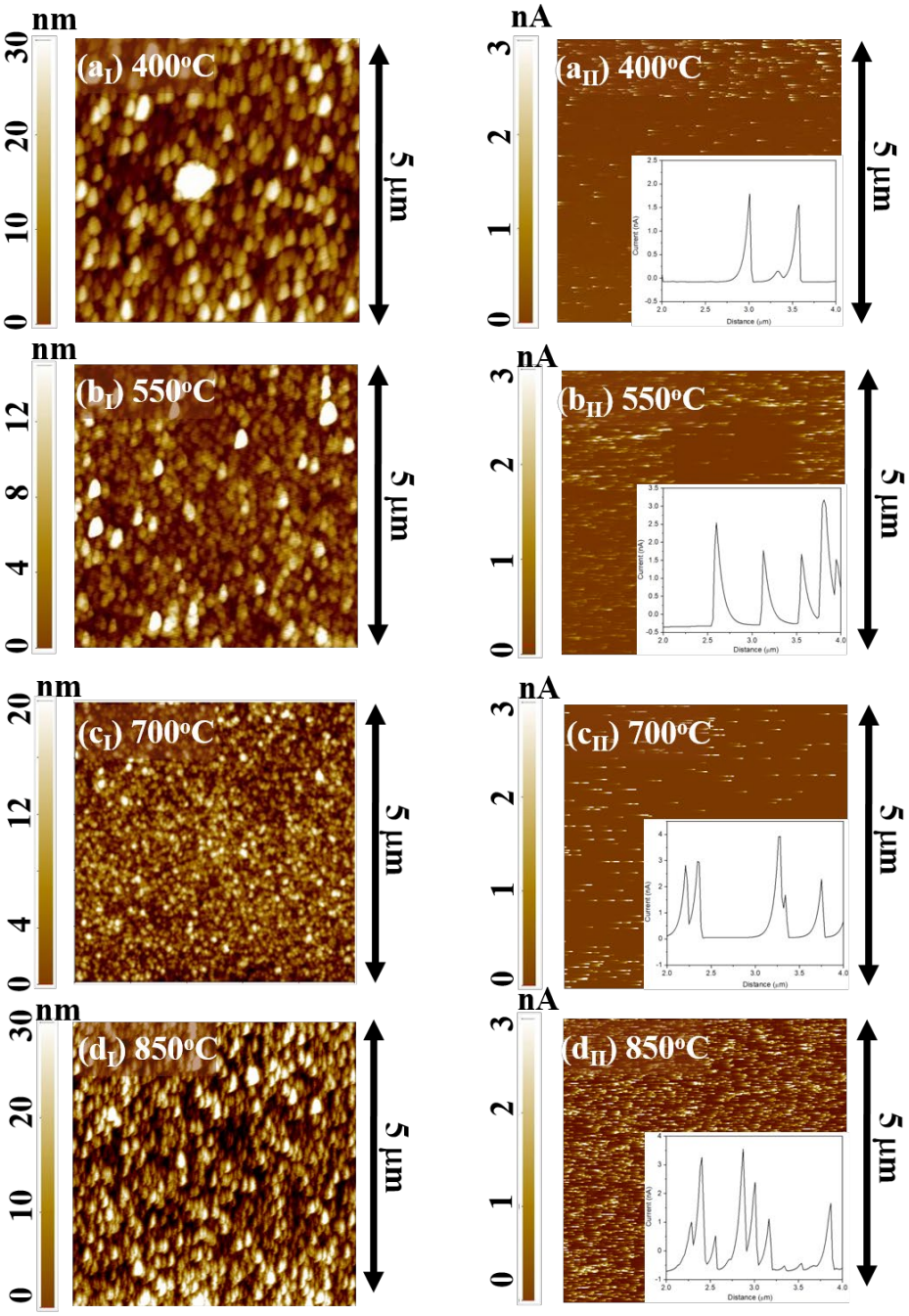

Figure 2.

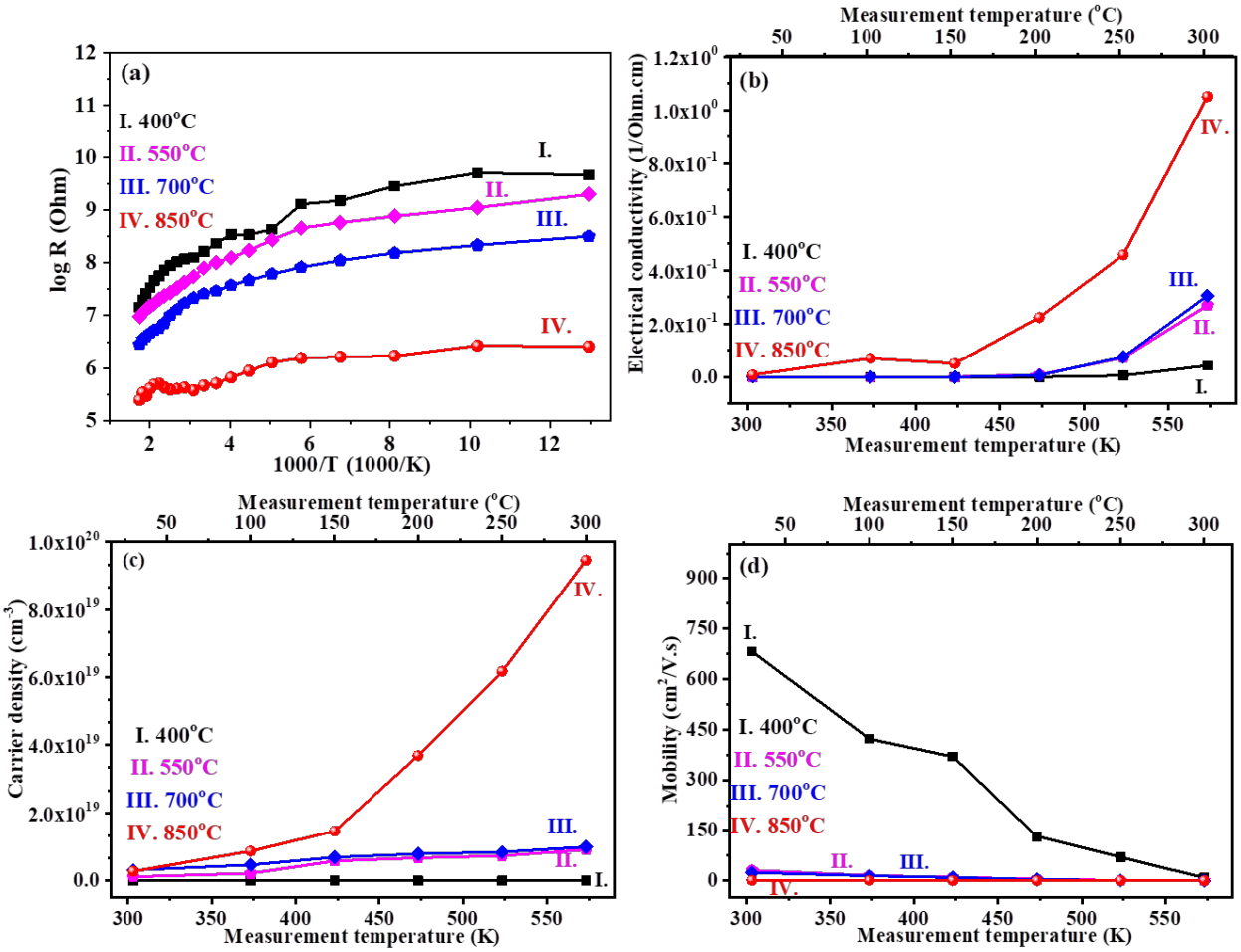

Figure 3.

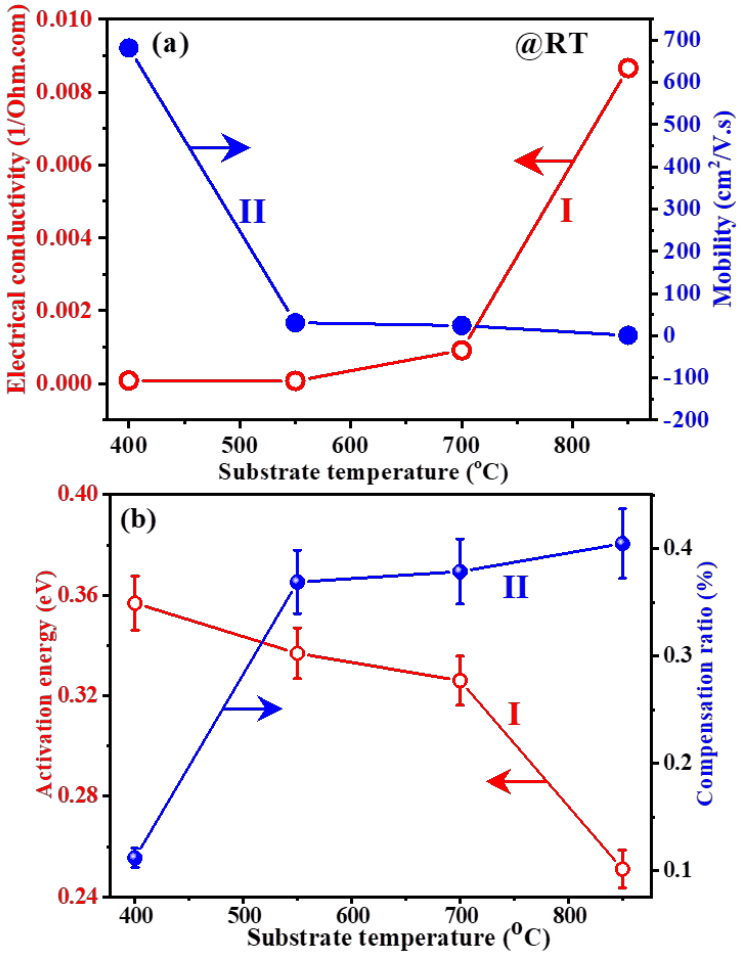

Figure 4.

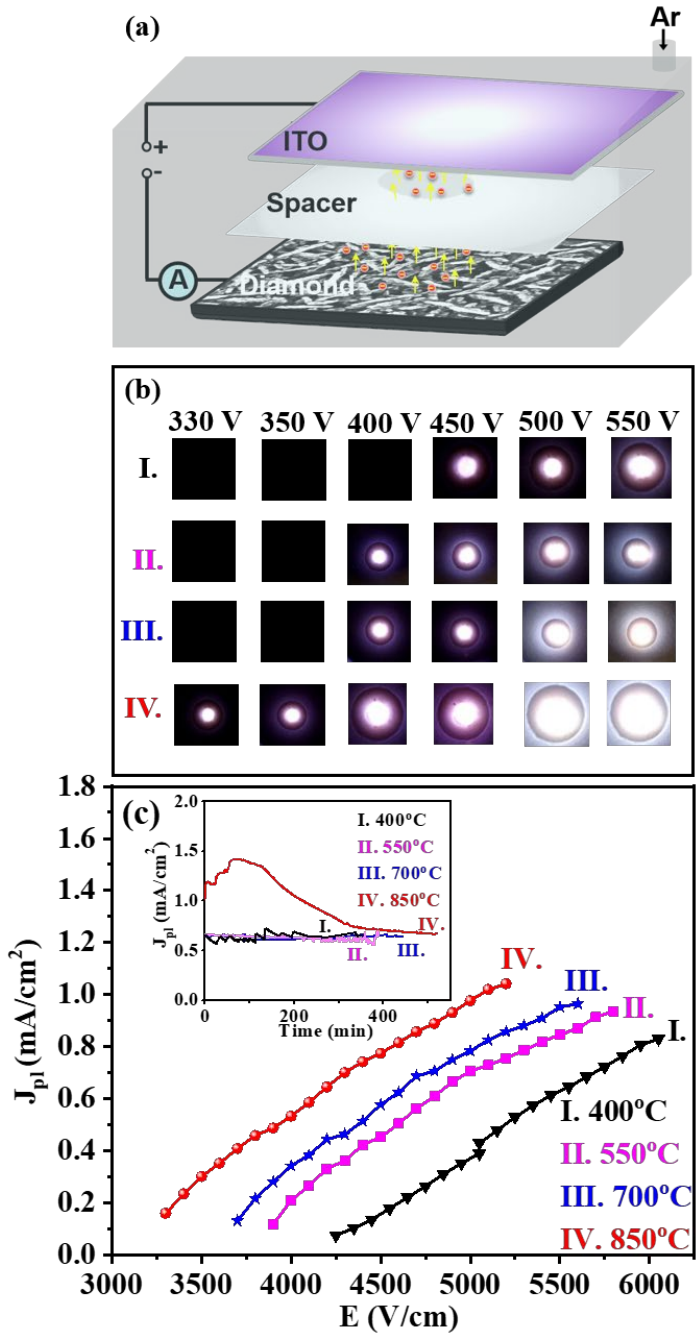

Figure 5.

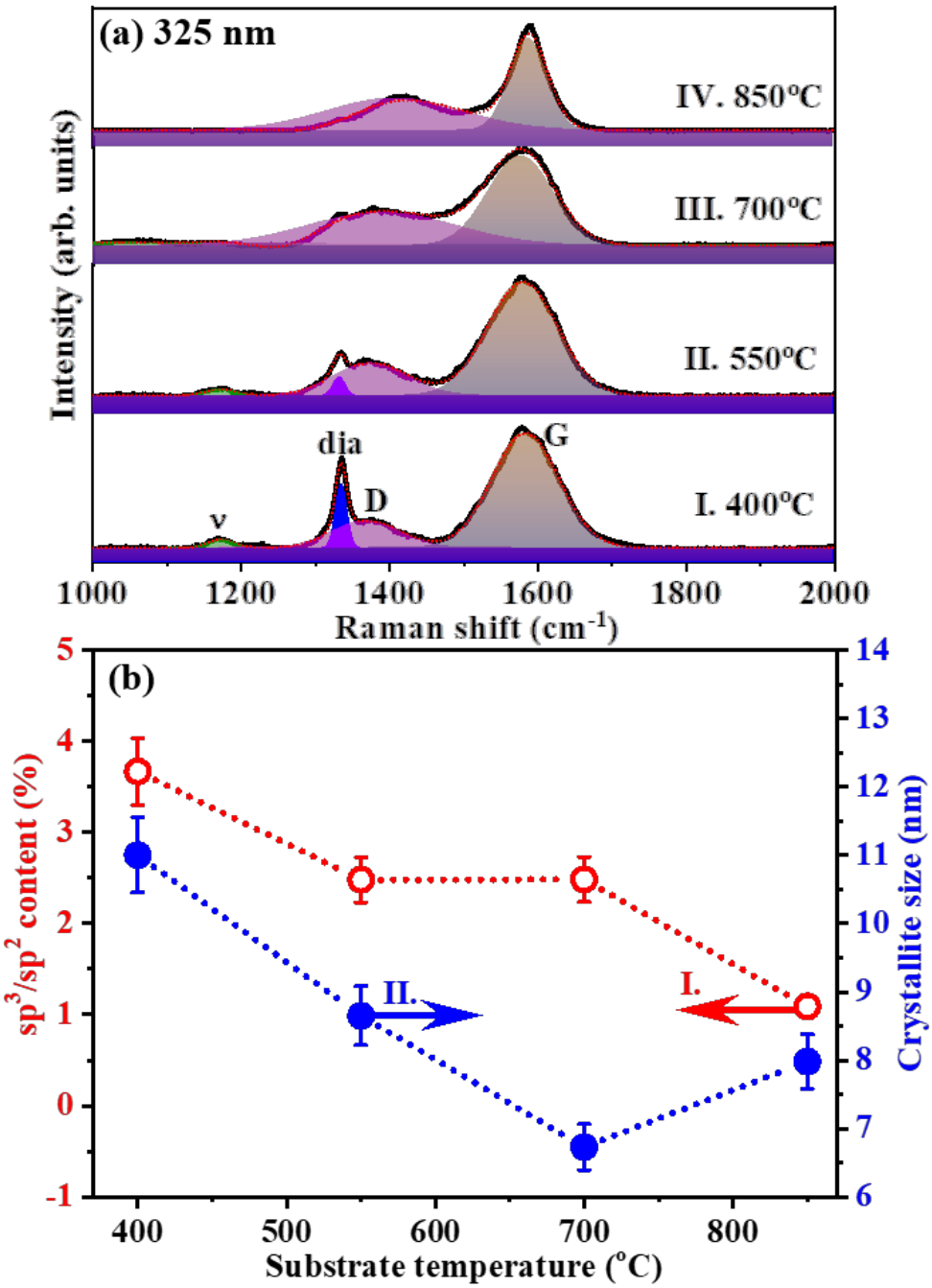

Figure 6.

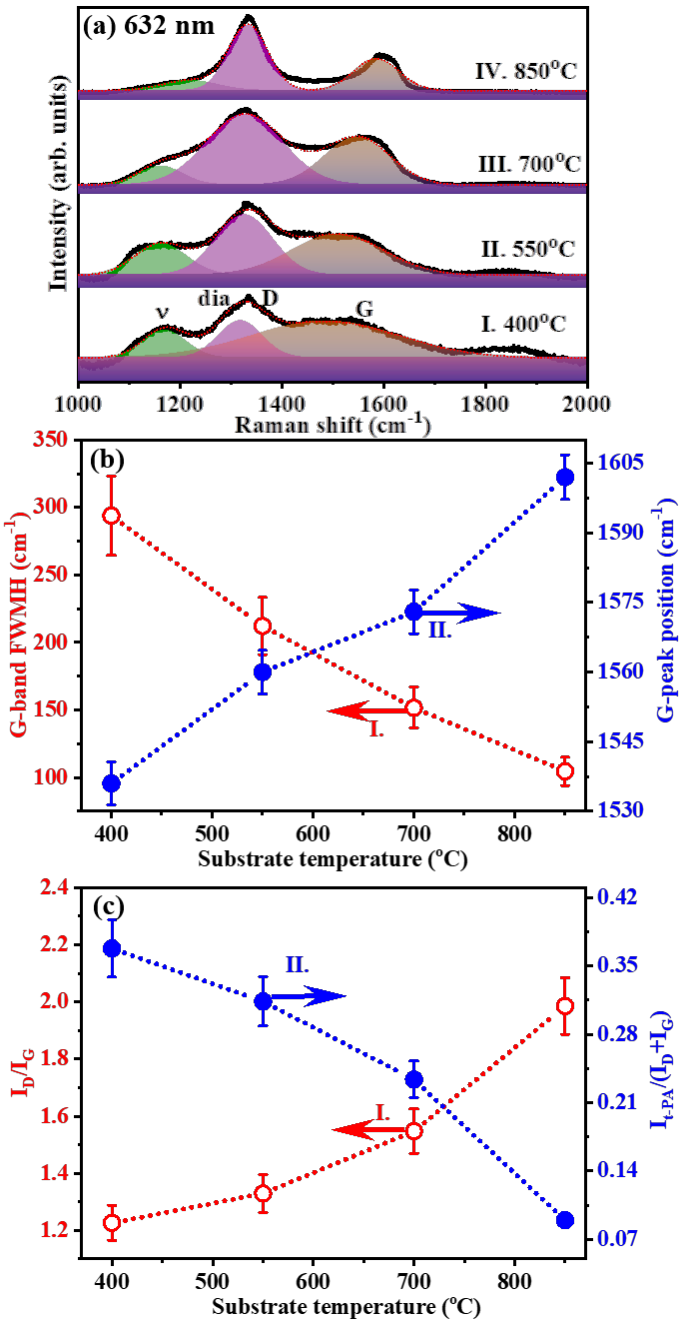

Figure 7.

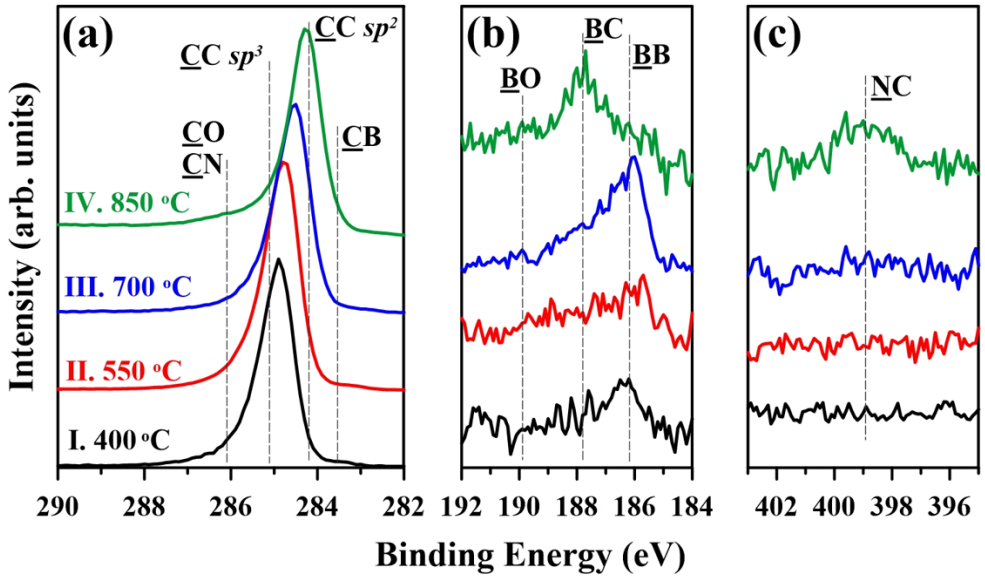

Figure 8.

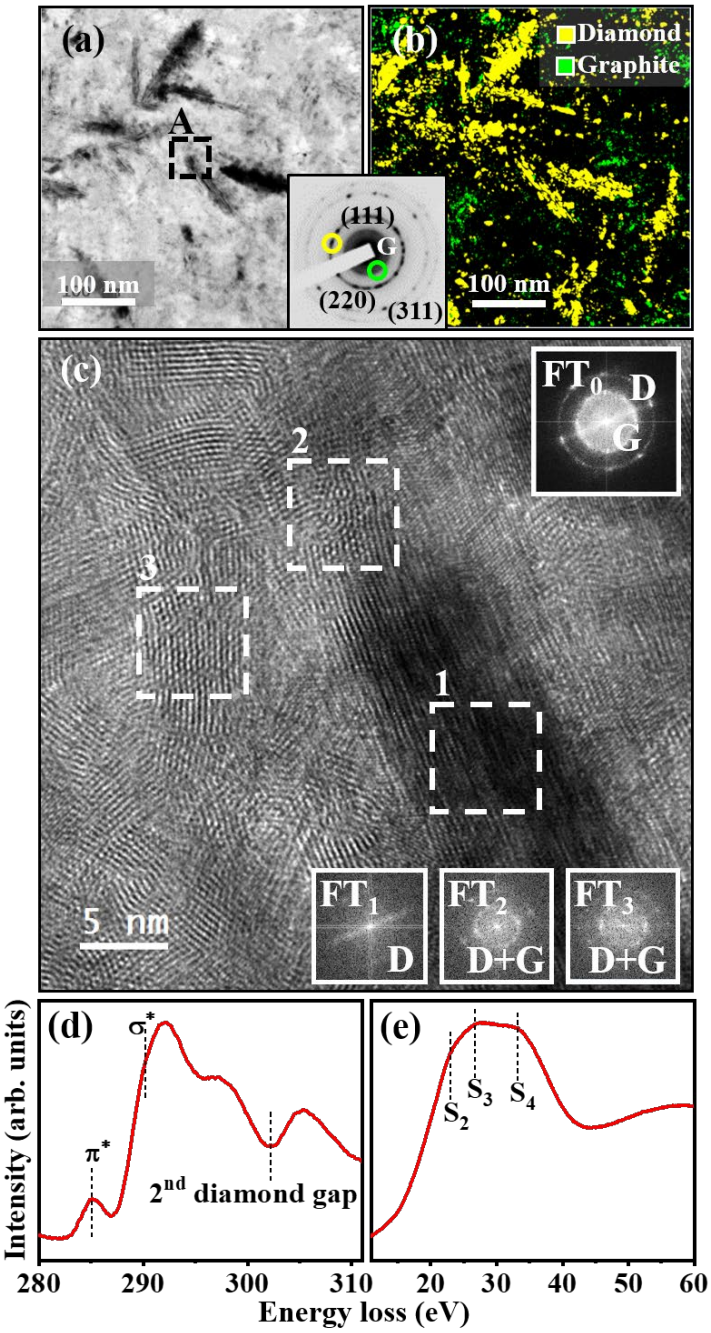

Figure 9.

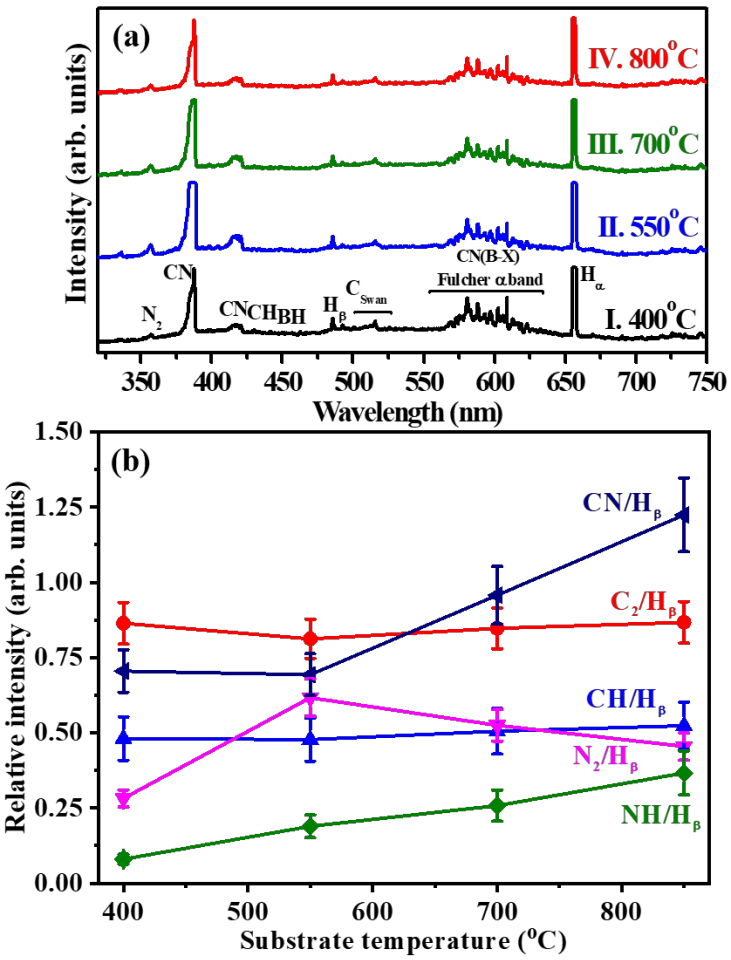

Figure 10.